

Supporting Information for “Scaling laws in Aeolian sand transport under low sand availability”

Sandesh Kamath^{1,2}, Yaping Shao¹, Eric J. R. Parteli²

¹Institute of Geophysics and Meteorology, University of Cologne, Germany

²Faculty of Physics, University of Duisburg-Essen, Germany

Contents of this file

Text S1 to S6

Figures S1 to S4

Table S1

Introduction

In this Supplemental Material, we briefly review the features of the Discrete-Element-Method referred to in the main document, including the complete set of the equations of motion, the details of the numerical integration of these equations, and the models of particle-particle interactions adopted in the simulations of Aeolian sand transport. Furthermore, we present the results of our numerical simulations performed to verify our model, the vertical profiles of the wind velocity and grain-borne shear stress during steady-state transport, and the behavior of the transport layer thickness as a function of the thickness of mobile sand layer, as mentioned in the main document.

S1 Discrete-Element-Method

In the Discrete-Element-Method, the equations of motion are solved for every particle in the system under consideration of the main forces acting on them. These forces are, in the process of non-suspended Aeolian transport of cohesionless particles, the drag force, the inter-particle contact forces and the gravitational force.

S1.1 Equations of motion and contact force model for the sand particles

The equation of translational motion for a particle of mass m_i at position \mathbf{r}_i reads,

$$m_i \ddot{\mathbf{r}}_i = \mathbf{F}_i^d + m_i \mathbf{g} + \sum_{\substack{1 \leq j \leq N_p \\ j \neq i}} \mathbf{F}_{ij}^c \quad (1)$$

where \mathbf{F}_i^d is the drag force on particle i , computed with the model described in the main document, \mathbf{g} is gravity, N_p is the number of particles in the system, j denotes the index of a neighbouring particle that is in contact with particle i , and \mathbf{F}_{ij}^c denotes the contact force exerted by particle j on i (with $\mathbf{F}_{ij}^c = -\mathbf{F}_{ji}^c$).

Contact between particles j and i occurs with their center-to-center distance is smaller than the sum of their radii, i.e., the contact force acts only if the particles overlap. To model the

Corresponding author: Sandesh Kamath, skamath@uni-koeln.de

33 contact force, the following equation is used to define the overlap,

$$34 \quad \delta_{ij,n} = \min \left\{ 0, \frac{1}{2} [d_i + d_j] - (\mathbf{r}_i - \mathbf{r}_j) \cdot \mathbf{e}_{ij,n} \right\} \quad (2)$$

35 where d_i and d_j are the diameters of particles i and j , respectively, $\mathbf{r}_{ij} = \mathbf{r}_i - \mathbf{r}_j$, with \mathbf{r}_j
 36 standing for the position of particle j , and $\mathbf{e}_{ij,n} = \mathbf{r}_{ij}/r_{ij}$ denotes the normal unit vector
 37 pointing from the center of particle j to the center of particle i , with $r_{ij} = |\mathbf{r}_{ij}|$.

38 There are various contact force models for application in DEM simulations, and the mod-
 39 elling of these forces is still an active matter of research (Cundall & Strack, 1979; Schäfer et
 40 al., 1996; Brilliantov et al., 1996; Silbert et al., 2001; Di Renzo & Di Maio, 2004; Pöschel &
 41 Schwager, 2005; Kruggel-Emden et al., 2007; Luding, 2008; Machado et al., 2012; Parteli et
 42 al., 2014; Fan et al., 2017; Schmidt et al., 2020; Santos et al., 2020). In our simulations, we
 43 adopt the linear spring-dashpot model, because this model has been employed in previous
 44 simulations of wind-blown sand that reproduced the scaling laws associated with Aeolian
 45 transport over fully erodible beds (Carneiro et al., 2011, 2013; Durán et al., 2012; Comola
 46 et al., 2019).

47 Specifically, \mathbf{F}_{ij}^c can be described as the sum of a normal component, $\mathbf{F}_{ij,n}^c$, and a tangential
 48 component, $\mathbf{F}_{ij,t}^c$. Each of these components encodes an elastic term and a dissipative term,
 49 while the magnitude of the tangential force is bounded by the Coulomb friction criterion.
 50 The equations for $\mathbf{F}_{ij,n}^c$ and $\mathbf{F}_{ij,t}^c$ read (Cundall & Strack, 1979; Silbert et al., 2001; Santos
 51 et al., 2020)

$$52 \quad \mathbf{F}_{ij,n}^c = k_n \delta_{ij,n} \mathbf{e}_{ij,n} - \gamma_n m_{\text{eff}} \mathbf{v}_{ij,n} \quad (3)$$

$$53 \quad \mathbf{F}_{ij,t}^c = -\min \left\{ \mu_s |\mathbf{F}_{ij,n}^c|, k_t \xi_{ij,t} + \gamma_t m_{\text{eff}} |\mathbf{v}_{ij,t}| \right\} \frac{\mathbf{v}_{ij,t}}{|\mathbf{v}_{ij,t}|} \quad (4)$$

55 where $m_{\text{eff}} = m_i m_j / (m_i + m_j)$, with m_i and m_j denoting the masses of particles i and j ,
 56 respectively, k_n , k_t , γ_n , γ_t and μ_s are model parameters, discussed in Section S1.3 below,
 57 while the relative normal velocity $\mathbf{v}_{ij,n}$ and the relative tangential velocity $\mathbf{v}_{ij,t}$ between
 58 particles i and j are computed via

$$59 \quad \mathbf{v}_{ij,n} = (\mathbf{v}_{ij} \cdot \mathbf{e}_{ij,n}) \mathbf{e}_{ij,n} \quad (5)$$

$$60 \quad \mathbf{v}_{ij,t} = \mathbf{v}_{ij} - \mathbf{v}_{ij,n} - \frac{1}{2} (\boldsymbol{\omega}_i + \boldsymbol{\omega}_j) \times (\mathbf{r}_i - \mathbf{r}_j) \quad (6)$$

62 with $\mathbf{v}_{ij} = \mathbf{v}_i - \mathbf{v}_j$ denoting the difference between the velocities of particles i and j (\mathbf{v}_i
 63 and \mathbf{v}_j , respectively), and $\boldsymbol{\omega}_i$ and $\boldsymbol{\omega}_j$ standing for their respective rotational velocities.
 64 Moreover, in Eq. (4), $\xi_{ij,t}$ is the tangential displacement accumulated as the particles are
 65 in contact. The displacement is set as zero at initiation of the contact and is computed in
 66 the reference frame of the rotating particle pair to compensate for the effect of rigid body
 67 rotations, as described in detail in previous work (Silbert et al., 2001; Santos et al., 2020).

68 The equation of rotational motion for particle i reads

$$69 \quad I_i \boldsymbol{\omega}_i = \sum_{\substack{1 \leq j \leq N_p \\ j \neq i}} \mathbf{M}_{ij} \quad (7)$$

70 with $I_i = m_i d_i^2 / 10$ and $\boldsymbol{\omega}_i$ denoting the moment of inertia and the angular velocity of
 71 particle i , respectively, and \mathbf{M}_{ij} corresponding to the torque on particle i associated with
 72 $\mathbf{F}_{ij,t}^c$.

Table S1: Parameters of the Discrete-Element-Method.

parameter	symbol	value
elastic constant for normal contact	k_n	157 N m^{-1}
elastic constant for tangential contact	k_t	52 N m^{-1}
viscoelastic damping constant for normal contact	γ_n	0.2 kg s^{-1}
viscoelastic damping constant for tangential contact	γ_t	0.2 kg s^{-1}
Coulomb coefficient of friction	μ_s	0.3
particle diameter	d_i	$[160, 240] \mu\text{m}$
particle density	ρ_p	2650 kg m^{-3}

S1.2 Contact forces between mobile and rigid particles (non-erodible elements)

The contact forces between mobile sand particles and the rigid particles constituting the roughness elements of the bed are computed using the same model as in the previous section, but considering that the rigid particles have an infinite mass (Verbücheln et al., 2015). Specifically, the normal and tangential components of the contact force from a rigid particle j on a mobile particle i are computed with Eqs. (3) and (4), respectively, by setting $m_{\text{eff}} = m_i$. Furthermore, contact forces between rigid particles are not considered.

S1.3 Model parameters

Table S1 displays the values of the parameters in Eqs. (3) and (4), i.e., the elastic constants k_n and k_t , the damping coefficients γ_n and γ_t , and the Coulomb friction coefficient, μ_s . The elastic and damping constants are taken from previous models for Aeolian sand transport over fully erodible beds (Carneiro et al., 2011, 2013; Comola et al., 2019). In particular, the elastic constant for normal contact, k_n , is estimated using $k_n = \pi d_m Y/4$, where $d_m = 200 \mu\text{m}$ is the mean particle size adopted in our simulations, while $Y = 1 \text{ MPa}$ is the Young’s modulus adopted in previous work (Carneiro et al., 2011; Comola et al., 2019) and in our computations. Furthermore, for the elastic constant for tangential constant, we use $k_t = k_n/3$, while the friction coefficient is consistent with values adopted previously (Comola et al., 2019).

S1.4 Numerical implementation and particle-wind coupling

To solve the equations of motion of the granular phase, we employ LAMMPS (Large-scale Atomic/Molecular Massively Parallel Simulator), which is an open source DEM solver based on MPI implementation (Plimpton, 1995). Furthermore, we have extended this solver to incorporate the hydrodynamic description of the turbulent wind flow over the granular surface, developed in previous work (Carneiro et al., 2011; Durán et al., 2012) and briefly reviewed in the main document. To this end, we have included new modules (LAMMPS “fixes”) into the granular package of the DEM solver, to set the initial (logarithmic) vertical profile of the mean horizontal wind speed, to compute the drag force, and to update this drag force and the wind profile owing to the process of momentum exchange between the particles and the wind. These modules are available from the corresponding author upon request.

S2 Validation of our simulations over fully erodible beds

To verify our numerical simulations, we compare our numerical predictions for the height-integrated mass flux (Q) of wind-blown particles over a fully erodible bed with corresponding wind-tunnel observations of this flux as a function of the wind shear velocity, u_* . We compute Q using the following equation,

$$Q = \frac{\sum_i^N m_i v_i^x}{A} \quad (8)$$

where N is the number of particles in the system, m_i and v_i^x denote the mass and horizontal speed of the i -th particle, respectively, and $A = L_x \cdot L_y$ is the horizontal area of the simulation domain. To measure this flux, we start the wind-blown transport process as described in the main document and wait until this transport achieves steady state. The typical (physical) time separating the begin of wind-blown transport from the steady state is about 2-3 seconds and independent of u_* (Carneiro et al., 2011; Durán et al., 2012; Pähz et al., 2014; Comola et al., 2019). All results reported in the present work refer to the characteristics of steady-state wind-blown transport, and denote mean quantities obtained from averaging over about 5-10 seconds during steady-state transport.

Furthermore, by suitably normalizing the steady-state flux Q , we obtain the following non-dimensional quantity,

$$\hat{Q} = \frac{Q}{\rho_p \sqrt{(s-1)gd_m^3}}, \text{ with } s = \frac{\rho_p}{\rho_f}, \quad (9)$$

which we plot in Fig. S1 as a function of the Shields number,

$$\Theta = \frac{u_*^2 \rho_f}{(\rho_p - \rho_f)gd_m} \quad (10)$$

where $\rho_p = 2650 \text{ kg/m}^3$ and $\rho_f = 1.225 \text{ kg/m}^3$ denote the densities of the particles and the air, respectively, while $d_m = 200 \mu\text{m}$ is the mean particle diameter and $g = 9.81 \text{ m/s}^2$ is gravity.

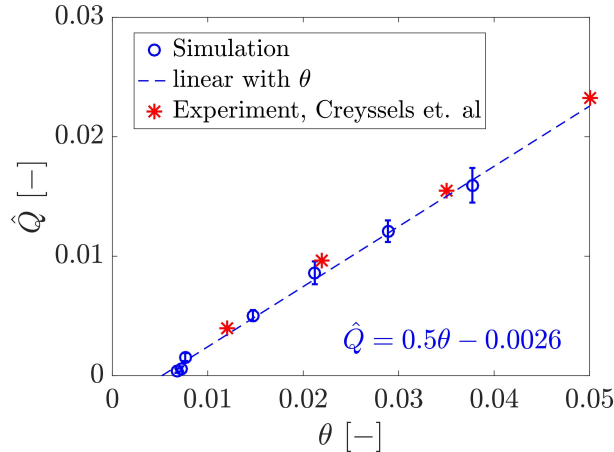


Figure S1: Normalized steady-state flux \hat{Q} as a function of the Shields number Θ , considering a fully erodible bed ($\delta_0 \approx 15 d_m$).

We see in Fig. S1 that our numerical predictions for $\hat{Q}(\Theta)$ (circles) agree quantitatively well with observations from wind-tunnel experiments (Creyssels et al., 2009), denoted by the stars. The best fit to our simulation results using $\hat{Q} = a\Theta + b$ yields $a \approx 0.5$ and $b \approx 0.0026$ (dashed line in Fig. S1), from which obtain the minimal threshold $\Theta_t \approx 0.0064$ below which

131 no transport occurs ($\hat{Q} = 0$). From Eq. (10), this value of Θ_t leads to the minimal threshold
 132 wind shear velocity for sustained transport, $u_{*t} \approx 0.165$ m/s.

133 We note that the value of u_{*t} predicted from our simulations is consistent with the prediction
 134 that u_{*t} is about 80% of the minimal threshold wind shear velocity u_{*ft} required to initiate
 135 transport,

$$136 \quad u_{*ft} = A_{ft} \sqrt{\frac{\rho_p - \rho_f}{\rho_f} g d_m}, \quad (11)$$

137 with $A_{ft} \approx 0.1$ (Bagnold, 1941; Shao & Lu, 2000). Indeed, by applying the mean particle
 138 size $d_m = 200 \mu\text{m}$ of our simulations in Eq. (11), we obtain $u_{*ft} \approx 0.206$ m/s, i.e., our model
 139 is consistent with the relation $u_{*t} \approx 0.8 u_{*ft}$ predicted for wind-blown transport.

140 S3 The modified wind profiles for varying δ_0

141 The initial vertical profile of the horizontal downstream wind velocity u_x is logarithmic and
 142 follows Eq. (3) of the main document. However, this wind velocity profile is updated every
 143 time-step, since the acceleration of the grains extracts momentum from the air thus creating
 144 a negative feedback on the wind. The modification of the wind velocity profile is computed
 145 using Eqs. (4) and (5) in the main document. The vertical profiles of the modified wind
 146 velocity u_x and the grain-borne shear stress τ_p are shown for different values of the mobile
 layer thickness δ_0 in Fig. S2.

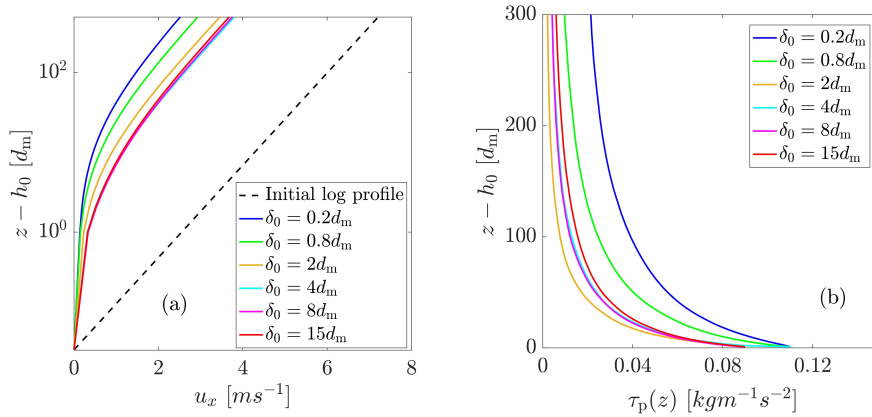


Figure S2: (a) The modified wind profiles for different values of δ_0 alongside the initial logarithmic profile; (b) grain-borne shear stress profile as a function of the height above the bed for different δ_0 . The results were obtained with $u_* = 0.30$ m/s.

147

148 S4 Computation of the mean hop length and the mean horizontal impact 149 and lift-off velocities

150 To compute the mean hop length ℓ_{hop} and the average horizontal impact and lift-off veloc-
 151 ities, $u_{0\downarrow}$ and $u_{0\uparrow}$, respectively, we consider only the grains with a minimum vertical lift-off
 152 velocity of $\sqrt{6gd}$, i.e., the grains that achieve a minimum height of $3d_m$ above the bed
 153 height. The values of ℓ_{hop} , $u_{0\downarrow}$ and $u_{0\uparrow}$, are then averaged over a time window of 5 seconds
 154 during steady-state sand transport.

155 The mean horizontal grain velocity or slip velocity u_0 is then computed using

$$156 \quad u_0 = (u_{0\downarrow} + u_{0\uparrow})/2. \quad (12)$$

157 Furthermore, to obtain the mean hop length, we start from the mean hop time, which is
 158 given by (Ho et al., 2011),

$$159 \quad t_{\text{hop}} \approx \frac{2v_{0\uparrow}}{g}, \quad (13)$$

160 where $v_{0\uparrow}$ is the mean ascending vertical velocity of the grains (also averaged over 5 seconds
 161 in the steady state). Furthermore, the horizontal acceleration of the grains is given by,

$$162 \quad a_{\text{hor}} \approx \frac{(u_{0\downarrow} - u_{0\uparrow})}{t_{\text{hop}}}, \quad (14)$$

163 so that the mean hop length is approximated as,

$$164 \quad \ell_{\text{hop}} \approx (u_{0\downarrow} - u_{0\uparrow}) \frac{v_{0\uparrow}}{g}. \quad (15)$$

165

166 **S5 Relation between the steady-state bed layer thickness, δ_s , and the** 167 **initial bed layer thickness, δ_0**

168 As mentioned in the main document, once the sand transport process begins, the initial
 169 thickness of the mobile sand bed applied in the numerical simulations, δ_0 , decreases toward
 170 a smaller value δ_s , which is achieved when transport conditions have reached steady state.
 171 As depicted in Fig. S3, δ_s and δ_0 are linearly related to each other, and the difference between
 172 both values of bed thickness displays a slight increase with u_* owing to the effect of wind
 173 shear velocity on enhancing erosion. However, we find that the scaling laws reported in
 174 the main document are valid whatever value of bed thickness is chosen, while the following
 175 relation applies,

$$176 \quad \frac{\delta_s}{d_m} = \left(\frac{\delta_0}{d_m} - C_b \frac{u_*}{\sqrt{gd_m}} \right) \cdot \Theta \left(\frac{\delta_0}{d_m} - C_b \frac{u_*}{\sqrt{gd_m}} \right) \quad (16)$$

177 where $C_b \approx 0.02$ is an empirical parameter and $\Theta(x)$ denotes the Heaviside function, i.e.,
 178 $\Theta(x) = 1$ if $x \geq 0$ and $\Theta(x) = 0$ if $x < 0$. Therefore, the term $C_b u_* / (\sqrt{gd_m})$ denotes
 179 the thickness of the total eroded layer, relative to the particle size, from the beginning of
 180 transport until steady state (i.e., as the bed thickness evolves from δ_0 toward δ_s).

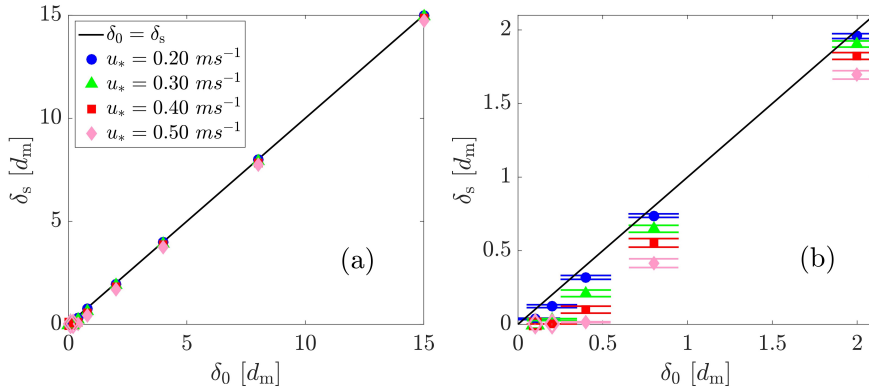


Figure S3: (a) Values of the bed layer thickness at steady-state transport, δ_s , plotted against the initial values of bed layer thickness, δ_0 , for different values of the wind shear velocity u_* . The plot in (b) denotes a zoom into the region of bed layer thickness comparable to the particle size. Filled symbols correspond to saturated transport conditions, while empty symbols denote under-saturated scenarios (the same color code used for the filled symbols in the legend applies to specify u_* in these empty symbol scenarios).

181 In Fig. S3, the filled symbols correspond to numerical simulations in which the wind is
 182 carrying the maximum possible number of particles, i.e., the flux is saturated. Starting
 183 with $\delta_0 = 15 d_m$, for instance, and under a given value of $u_* - u_{*t}$, we observe no change in
 184 the average number of particles in the Aeolian layer (or, equivalently, the mass density of
 185 dragged particles) upon a decrease in the initial bed thickness δ_0 , as long as the scenarios
 186 associated with the filled symbols in Fig. S3 are considered. However, the empty symbols
 187 in this figure constitute scenarios where the bed thickness is so small, that the wind flow
 188 does not dispose of enough particles on the ground to drive transport toward the saturated
 189 flux. These empty symbols are associated with a value of steady-state bed thickness equal
 190 to 0 and are referred to as *under-saturated*. Specifically, for these empty symbols, the wind
 191 eroded the entire sand bed and still the amount of sand transport is not enough to saturate
 192 the sand flux (the most extreme, non-vanishing flux scenario of such under-saturated regime
 193 in our simulations would be, in particular, the case of one single grain hopping downwind).

194 We have thus not considered these under-saturated scenarios in our analysis of $Q(u_*)$ in
 195 the main document, since we are interested here in an expression for the saturated flux
 196 that accounts for the bed erodibility. Moreover, it is a straightforward conclusion that,
 197 in the under-saturated regime, the mass density of the transport layer decreases upon a
 198 reduction of the initial bed thickness δ_0/d_m . Nevertheless, we note that under-saturated
 199 transport scenarios constitute an interesting topic to be investigated in future work. For
 200 instance, such scenarios have applications to areas that are devoid of any sand availability
 201 but subjected to an upwind flux that is under-saturated (for instance in the presence of
 202 upwind vegetation or moisture), or over inter-dune bedrock areas within fields of sparsely
 203 distributed dunes (Fryberger et al., 1984)).

204 S6 Transport layer thickness as a function of the bed thickness

205 As explained in the main document, the transport layer expands gradually as the soil erodi-
 206 bility conditions change from fully erodible to rigid. To quantify this process, we compute
 207 the characteristic length-scale l_ν associated with the nearly exponential decay of the particle
 208 concentration $\nu(z)$ with the height z above the ground, i.e.,

$$209 \nu(z) = \nu_0 \exp(-z/l_\nu) \quad (17)$$

210 where ν_0 is the particle concentration extrapolated to the bed ($z = 0$). Fig. S4 shows the
 211 behavior of l_ν as a function of the thickness of mobile sand layer on the ground, δ_0 . We see
 212 that, when the rigid ground is flat, l_ν decreases monotonically as δ_0 increases toward $15 d_m$
 213 (the fully erodible bed scenario). However, when the rigid surface is armoured with non-
 214 erodible elements (which in our simulations have the same size as the mobile particles), a
 215 minimum in l_ν is observed near $\delta_0 = 2 d_m$. This minimum can be explained by the prevailing
 216 occurrence of backward ejecta in the range $\delta_0 \lesssim 2 d_m$ (as described in the main document),
 217 which leads to lower values of l_ν in this range when non-erodible particles cover the ground,
 218 compared to the flat ground scenario. As δ_0 becomes much larger than the particle size, the
 219 effect of the immobile particles on the Aeolian transport thickness becomes negligible, and
 220 l_ν approaches asymptotically the value corresponding to the fully erodible bed as shown in
 221 Fig. S4.

222 References

- 223 Bagnold, R. A. (1941). *The physics of blown sand and desert dunes*. Methuen, London.
 224 Brilliantov, N. V., Spahn, F., Hertzsch, J.-M., & Pöschel, T. (1996). Model for collisions
 225 in granular gases. *Physical review E*, *53*(5), 5382. doi: [https://doi.org/10.1103/](https://doi.org/10.1103/PhysRevE.53.5382)
 226 [PhysRevE.53.5382](https://doi.org/10.1103/PhysRevE.53.5382)
 227 Carneiro, M. V., Araújo, N. A. M., Pähltz, T., & Herrmann, H. J. (2013). Midair collisions
 228 enhance saltation. *Physical review letters*, *111*(5), 058001. doi: [https://doi.org/](https://doi.org/10.1103/PhysRevLett.111.058001)
 229 [10.1103/PhysRevLett.111.058001](https://doi.org/10.1103/PhysRevLett.111.058001)

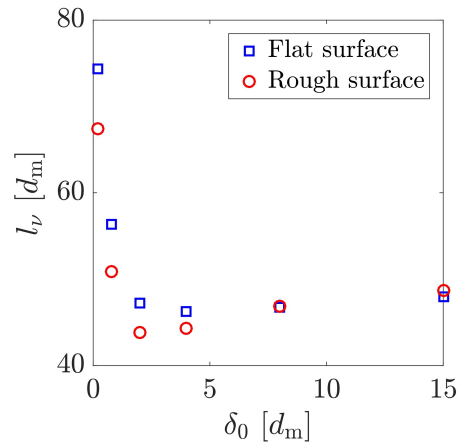


Figure S4: Thickness l_ν of the transport layer as a function of the thickness δ_0 of the mobile sediment layer covering the non-erodible surface, which consists of a flat horizontal surface (blue symbols) and a sheet of immobile particles (red symbols). The results were obtained with $u_* = 0.30$ m/s.

- 230 Carneiro, M. V., Pähtz, T., & Herrmann, H. J. (2011). Jump at the onset of saltation.
 231 *Physical Review Letters*, *107*(9), 098001. doi: [https://doi.org/10.1103/PhysRevLett](https://doi.org/10.1103/PhysRevLett.107.098001)
 232 [.107.098001](https://doi.org/10.1103/PhysRevLett.107.098001)
- 233 Comola, F., Gaume, J., Kok, J., & Lehning, M. (2019). Cohesion-induced enhancement
 234 of aeolian saltation. *Geophysical Research Letters*, *46*(10), 5566–5574. doi: [https://](https://doi.org/10.1029/2019GL082195)
 235 doi.org/10.1029/2019GL082195
- 236 Creyssels, M., Dupont, P., El Moctar, A. O., Valance, A., Cantat, I., Jenkins, J. T., ...
 237 Rasmussen, K. R. (2009). Saltating particles in a turbulent boundary layer: ex-
 238 periment and theory. *J. Fluid Mechanics*, *625*, 47. doi: [https://doi.org/10.1017/](https://doi.org/10.1017/S0022112008005491)
 239 [S0022112008005491](https://doi.org/10.1017/S0022112008005491)
- 240 Cundall, P. A., & Strack, O. D. (1979). A discrete numerical model for granular assemblies.
 241 *geotechnique*, *29*(1), 47–65. doi: <https://doi.org/10.1680/geot.1979.29.1.47>
- 242 Di Renzo, A., & Di Maio, F. P. (2004). Comparison of contact-force models for the simulation
 243 of collisions in dem-based granular flow codes. *Chemical Engineering Science*, *59*(3),
 244 525–541. doi: <https://doi.org/10.1016/j.ces.2003.09.037>
- 245 Durán, O., Andreotti, B., & Claudin, P. (2012). Numerical simulation of turbulent sediment
 246 transport, from bed load to saltation. *Physics of Fluids*, *24*(10), 103306. doi: [https://](https://doi.org/10.1063/1.4757662)
 247 doi.org/10.1063/1.4757662
- 248 Fan, F., Parteli, E. J. R., & Pöschel, T. (2017). Origin of granular capillarity revealed
 249 by particle-based simulations. *Phys. Rev. Lett.*, *118*, 218001. doi: [https://doi.org/](https://doi.org/10.1103/PhysRevLett.118.218001)
 250 [10.1103/PhysRevLett.118.218001](https://doi.org/10.1103/PhysRevLett.118.218001)
- 251 Fryberger, S. G., Al-Sari, A. M., Clisham, T. J., Rizvi, S. A. R., & Al-Hinai, K. G. (1984).
 252 Wind sedimentation in the jafurah sand sea, saudi arabia. *Sedimentology*, *31*, 413–431.
 253 doi: <https://doi.org/10.1111/j.1365-3091.1984.tb00869.x>
- 254 Ho, T. D., Valance, A., Dupont, P., & El Moctar, A. O. (2011). Scaling laws in aeolian sand
 255 transport. *Physical Review Letters*, *106*(9), 094501. doi: [https://doi.org/10.1103/](https://doi.org/10.1103/PhysRevLett.106.094501)
 256 [PhysRevLett.106.094501](https://doi.org/10.1103/PhysRevLett.106.094501)
- 257 Kruggel-Emden, H., Simsek, E., Rickelt, S., Wirtz, S., & Scherer, V. (2007). Review and
 258 extension of normal force models for the discrete element method. *Powder Technol.*,
 259 *171*, 157–173. doi: <https://doi.org/10.1016/j.powtec.2006.10.004>
- 260 Luding, S. (2008). Cohesive, frictional powders: contact models for tension. *Granular*
 261 *matter*, *10*(4), 235. doi: <https://doi.org/10.1007/s10035-008-0099-x>

- 262 Machado, M., Moreira, P., Flores, P., & Lankarani, H. M. (2012). Compliant contact force
 263 models in multibody dynamics: Evolution of the hertz contact theory. *Mechanism and*
 264 *Machine Theory*, *53*, 99-121. doi: <https://doi.org/10.1016/j.mechmachtheory.2012.02>
 265 .010
- 266 Pähitz, T., Parteli, E. J. R., Kok, J. F., & Herrmann, H. J. (2014). Analytical model
 267 for flux saturation in sediment transport. *Physical Review E*, *89*(5), 052213. doi:
 268 <https://doi.org/10.1103/PhysRevE.89.052213>
- 269 Parteli, E. J. R., Schmidt, J., Blümel, C., Wirth, K.-E., Peukert, W., & Pöschel, T. (2014).
 270 Attractive particle interaction forces and packing density of fine glass powders. *Sci.*
 271 *Rep.*, *4*, 6227. doi: <https://doi.org/10.1038/srep06227>
- 272 Plimpton, S. (1995). Fast parallel algorithms for short-range molecular dynamics. *Journal of*
 273 *computational physics*, *117*(1), 1–19. (Website of the DEM solver LAMMPS: [https://](https://lammps.sandia.gov/)
 274 lammps.sandia.gov/) doi: <https://doi.org/10.1006/jcph.1995.1039>
- 275 Pöschel, T., & Schwager, T. (2005). *Computational granular dynamics*. Springer Berlin
 276 Heidelberg. doi: <https://doi.org/10.1007/3-540-27720-X>
- 277 Santos, A. P., Bolintineanu, D. S., Grest, G. S., Lechman, J. B., Plimpton, S. J., Srivastava,
 278 I., & Silbert, L. E. (2020). Granular packings with sliding, rolling, and twisting friction.
 279 *Phys. Rev. E*, *102*, 032903. doi: <https://doi.org/10.1103/PhysRevE.102.032903>
- 280 Schäfer, J., Dippel, S., & Wolf, D. E. (1996). Force Schemes in Simulations of Granular
 281 Materials. *J. Phys. I France*, *6*, 5-20. doi: <https://doi.org/10.1051/jp1:1996129>
- 282 Schmidt, J., Parteli, E. J., Uhlmann, N., Wörlein, N., Wirth, K.-E., Pöschel, T., & Peukert,
 283 W. (2020). Packings of micron-sized spherical particles: Insights from bulk density de-
 284 termination, x-ray microtomography and discrete element simulations. *Advanced Pow-*
 285 *der Technology*, *31*(6), 2293-2304. doi: <https://doi.org/10.1016/j.appt.2020.03.018>
- 286 Shao, Y., & Lu, H. (2000). A simple expression for wind erosion threshold friction velocity.
 287 *Journal of Geophysical Research: Atmospheres*, *105*(D17), 22437-22443. doi: [https://](https://doi.org/10.1029/2000JD900304)
 288 doi.org/10.1029/2000JD900304
- 289 Silbert, L. E., Ertas, D., Grest, G. S., Halsey, T. C., Levine, D., & Plimpton, S. J. (2001).
 290 Granular flow down an inclined plane: Bagnold scaling and rheology. *Physical Review*
 291 *E*, *64*(5), 051302. doi: <https://doi.org/10.1103/PhysRevE.64.051302>
- 292 Verbücheln, F., Parteli, E. J. R., & Pöschel, T. (2015). Helical inner-wall texture prevents
 293 jamming in granular pipe flows. *Soft Matter*, *11*(21), 4295–4305. doi: [https://doi.org/](https://doi.org/10.1039/c5sm00760g)
 294 [10.1039/c5sm00760g](https://doi.org/10.1039/c5sm00760g)